Trabid patient mutations impede the axonal trafficking of adenomatous polyposis coli to disrupt neurite growth

Daniel Frank[1,7,14], Maria Bergamasco[2,7,14], Michael Mlodzianoski[3,7,14], Andrew Kueh[4,7,8,9], Ellen Tsui[5,7], Cathrine Hall[6,7], Georgios Kastrappis[10], Anne Kathrin Voss[2,7], Catriona McLean[11], Maree Faux[12], Kelly Rogers[3,7], Bang Tran[10], Elizabeth Vincan[10,13], David Komander[1,7], Grant Dewson[1,7,15], and Hoanh Tran[1,7,10,15]

[1]Ubiquitin Signalling Division, [2]Epigenetics and Development Division, [3]Centre for Dynamic Imaging, [4]Melbourne Advanced Genome Editing Centre, [5]Histology Facility, [6]Inflammation Division, Walter and Eliza Hall Institute of Medical Research, Parkville, VIC 3052, Australia
[7]Department of Medical Biology, The University of Melbourne, Parkville, VIC 3052, Australia
[8]Olivia Newton-John Cancer Research Institute, Heidelberg, VIC 3084, Australia
[9]School of Cancer Medicine, La Trobe University, Heidelberg, VIC 3084, Australia
[10]Department of Infectious Diseases, The University of Melbourne at The Peter Doherty Institute for Infection and Immunity, Melbourne, VIC 3000, Australia
[11]Department of Anatomical Pathology, The Alfred Hospital, Melbourne, VIC 3004, Australia
[12]Neuro-Oncology Group, Murdoch Children's Research Institute, Parkville, VIC 3052, Australia
[13]The Victorian Infectious Diseases Reference Laboratory, Royal Melbourne Hospital at The Peter Doherty Institute for Infection and Immunity, Melbourne, VIC 3000, Australia
[14]These authors contributed equally to this work
[15]Corresponding authors dewson@wehi.edu.au, tran.h@wehi.edu.au

Running Title: Deubiquitylating enzyme Trabid controls polarised axon elongation

Abstract

Trabid/ZRANB1 missense mutations have been identified in children diagnosed with a range of congenital disorders including reduced brain size, but how Trabid regulates neurodevelopment is not understood. We have characterised these patient mutations in cells and mice to identify a key role for Trabid in the regulation of neurite growth. One of the patient mutations flanked the catalytic cysteine of Trabid and its deubiquitylating (DUB) activity was abrogated. The second variant retained DUB activity, but failed to bind STRIPAK, a large multiprotein assembly implicated in cytoskeleton organisation and neural development. *Trabid/ZRANB1* knock-in mice harbouring either of these patient mutations exhibited reduced neuronal and glial cell densities in the brain and a motor deficit consistent with fewer dopaminergic neurons and projections. Mechanistically, both DUB-impaired and STRIPAK-binding-deficient Trabid variants impeded the trafficking of adenomatous polyposis coli (APC) to microtubule plus-ends. Consequently, the formation of neuronal growth cones and the trajectory of neurite outgrowth from mutant midbrain progenitors were severely compromised. We propose that STRIPAK recruits Trabid to deubiquitylate APC, and that in cells with mutant Trabid, APC becomes hyperubiquitylated and mislocalised causing impaired organisation of the cytoskeleton that underlie the neuronal and developmental phenotypes.

Introduction

Deubiquitylating enzymes (DUBs) are integral components of the ubiquitin system that control protein functions essential for healthy development and aging (Clague et al. 2019). DUBs catalyze the removal of ubiquitin from protein substrates to regulate protein stability, activity, interaction, or localisation (Komander et al. 2009). Ubiquitin can be assembled into polymers linked through one of eight internal ubiquitin residues – Met1, Lys6, Lys11, Lys27, Lys29, Lys33, Lys48 and Lys63 – and impairment of DUB function can lead to the accumulation of one or more of these ubiquitin chain linkages on a protein substrate with deleterious consequences. For example, LINKage-specific deubiquitylation deficiency-induced Embryonic Defects (LINKED), a human syndrome caused by loss-of-function mutations in the DUB OTUD5, is associated with increased Lys48-linked ubiquitylation and turnover of chromatin remodeling and transcription factors that are critical for normal embryonic development (Beck et al. 2021).

63 Consequently, LINKED syndrome patients manifest severe congenital malformations and die in
64 early infancy (Beck et al. 2021). OTUD5 belongs to a 17-member family of human DUBs that
65 possess an OTU (*o*varian *tu*mour) catalytic domain and include the closely related OTU DUBs
66 A20, Cezanne and Trabid. Trabid missense mutations have been identified in children diagnosed
67 with a range of developmental disorders including microcephaly (Deciphering Developmental
68 Disorders 2015).
69
70 Trabid has two defining biochemical features. First, it exhibits strong DUB specificity for Lys29-
71 and Lys33-linked ubiquitin chains, cleaving these chain types 40-fold more efficiently than
72 Lys63-linked chains (Licchesi et al. 2012). Lys29-linked polyubiquitin exists mainly as
73 heterotypic chains containing Lys48 linkages that target substrates for degradation (Kristariyanto
74 et al. 2015; Leto et al. 2019; Harris et al. 2021). Trabid is thought to modulate the levels of
75 Lys29/Lys48 mixed chains to regulate proteostasis, autophagy and cell division (Chen et al.
76 2021; Yu et al. 2021; Vaughan et al. 2022). Lys33-linked ubiquitin polymers have been
77 implicated in post-Golgi protein trafficking (Yuan et al. 2014), and Lys63-linked chains are
78 abundant cellular adducts with established roles in the sorting of endosomal/lysosomal cargo
79 (Erpapazoglou et al. 2014) and mediating the formation of protein assemblies (Tran and Polakis
80 2012). The second defining feature of Trabid is that it binds the Striatin-interacting phosphatase
81 and kinase (STRIPAK) complex (Sowa et al. 2009; Tran et al. 2013; Harris et al. 2021), a large
82 multiprotein assembly implicated in cytoskeleton organisation, cell migration and neural
83 development (Hwang and Pallas 2014; Sakuma et al. 2014; Madsen et al. 2015; Bazzi et al.
84 2017; Kuck et al. 2019).
85
86 We have previously identified the adenomatous polyposis coli (APC) protein as a candidate
87 Trabid substrate (Tran et al. 2008). Trabid knockdown in HEK293 cells caused APC to become
88 modified with polyubiquitin and aggregate in the cytoplasm, whereas high Trabid levels
89 correlated with *hypo*ubiquitylated APC that accumulated in the membrane protrusions of long
90 cell processes. These observations led us to propose that Trabid regulates the ubiquitylation and
91 subcellular localisation of APC (Tran et al. 2013). In neurons, APC organises the cortical
92 cytoskeleton to promote the formation of growth cones and the steering of growing axons that
93 are essential for embryonic brain development (Yokota et al. 2009; Preitner et al. 2014;

94 Dogterom and Koenderink 2019; Efimova et al. 2020). High expression of Trabid, APC and
95 STRIPAK proteins in neural stem cells (Castets et al. 2000; Blanpain et al. 2004; Yokota et al.
96 2009) indicate that Trabid's association with STRIPAK and its ability to regulate APC
97 polyubiquitylation may be important for neurogenesis. We now show that two Trabid mutants
98 found in children with developmental deficits are impaired in two distinct biochemical activities
99 that culminate in the perturbed trafficking of APC to neurite tips. We propose that the neuronal
100 and developmental phenotypes associated with these Trabid loss-of-function mutations are
101 primarily caused by the mislocalisation of APC that leads to defective cytoskeleton organisation
102 and aberrant cell locomotion.
103
104
105 **Results**
106 **Trabid patient variants are impaired in DUB activity and STRIPAK binding**
107 *Trabid/ZRANB1* patient missense mutations, R438W and A451V, are linked to developmental
108 microcephaly (Deciphering Developmental Disorders 2015). Mapping these residues onto the
109 domain structure of Trabid show that they flank either side of Trabid's catalytic cysteine C443
110 (Fig. 1A). Residue R438 projects prominently into the catalytic cleft formed by the ankyrin
111 repeats and the OTU core of Trabid's catalytic domain (Licchesi et al. 2012), whereas residue
112 A451 resides at the back of the active site, opposite to C443 on alpha helix 4 (Fig. 1B). To
113 determine if patient mutations R438W and A451V influence substrate catalysis, we purified the
114 mutant AnkOTU domains and tested their ability to hydrolyse synthetic ubiquitin chains *in vitro*
115 (Licchesi et al. 2012). Wild-type Trabid AnkOTU generated appreciable amounts of mono-
116 ubiquitin within 15 min incubation with either Lys29- or Lys63-linked di-ubiquitin chains (Fig
117 1C and D). In contrast, Trabid R438W showed near total loss of DUB activity and cleaved
118 ubiquitin product was only readily detected after a prolonged 120 min incubation (Fig. 1C and
119 D). A catalytically inactive C443S mutant AnkOTU domain failed to hydrolyse ubiquitin chains
120 even after 2 h incubation (Fig. 1C and D). Interestingly, the Trabid A451V AnkOTU domain
121 cleaved Lys29- or Lys63-linked di-ubiquitin with comparable efficiency to wild-type Trabid,
122 despite it being slightly less stable as a recombinant protein based on thermal stability assay
123 (Supplementary Fig. 1A). A ubiquitin suicide probe assay revealed that R438W and A451V

124 Trabid AnkOTU proteins retained a functional catalytic interaction with ubiquitin
125 (Supplementary Fig. 1B).
126
127 In cells, the inability of the DUB-inactive Trabid C443S to cleave polyubiquitin led to stable
128 interaction of this mutant with polyubiquitylated substrates (Tran et al. 2008; Licchesi et al.
129 2012). We therefore asked whether the DUB-impaired R438W Trabid likewise exhibited
130 increased binding to polyubiquitin in cells. Polyubiquitin chains readily co-precipitated with both
131 FLAG-tagged Trabid R438W and FLAG-Trabid C443S expressed in HEK293T cells, consistent
132 with the compromised DUB activity of these mutants (Fig. 1E). The Trabid A451V variant did
133 not co-precipitate abundant polyubiquitylated substrates, consistent with it retaining full DUB
134 activity (Fig 1E).
135
136 We have previously identified an interaction between Trabid and STRIPAK that is important for
137 the deubiquitylation of substrate APC (Tran et al. 2013). Whilst A451V retained full DUB
138 activity, strikingly, in contrast to FLAG-Trabid wild-type, R438W and C443S, the FLAG-Trabid
139 A451V mutant failed to efficiently co-precipitate several STRIPAK components, including
140 Striatin3 and STRIP1 (Fig. 1E). All FLAG-Trabid proteins co-precipitated similar levels of the
141 substrate E3 ubiquitin ligase HECTD1 (Tran et al. 2013; Harris et al. 2021). Together, these
142 results suggest that the Trabid patient mutations produce hypomorphic variants impaired in two
143 distinct biochemical activities: polyubiquitin hydrolysis and STRIPAK-binding.
144
145 **Decreased cell density in the brains of mice harbouring Trabid patient mutations**
146 Given the microcephaly observed in children with Trabid mutations, and to understand the
147 consequence of Trabid hypomorphic variants *in vivo*, we examined knock-in mice carrying
148 Trabid patient mutations for evidence of brain development abnormalities (Fig. 2A). Mice
149 heterozygous or homozygous for the R438W or A451V mutation were viable, fertile, and born at
150 expected Mendelian ratios (Fig. 2B). Because germline Trabid knockout or C443S homozygous
151 knock-in mice exhibit perinatal lethality (Dickinson et al. 2016) (our unpublished data), these
152 new R438W and A451V mutant mouse strains allow us to interrogate Trabid function *in vivo*.
153 Homozygous mutant mice from the R438W colony weighed on average ~15% less than wild-
154 type littermates, while R438W heterozygous and A451V mutant mice did not exhibit significant

155 weight loss (Fig. 2C). Immunohistochemical analysis of brain sections from weaned littermate
156 mice of both mutant strains revealed normal structure and laminar organisation of the cerebral
157 cortex, but intriguingly a reduction in cell number was apparent in different brain regions of
158 R438W and A451V homozygous mice compared to wild-type littermate controls (Fig. 2D). The
159 number of Ctip2+ medium spiny neurons in the striatum of R438W and A451V mutant mice
160 were reduced compared with wild-type littermates, and homozygous mice showed a greater cell
161 number loss than heterozygous mice, suggesting a gene dosage effect (Fig. 2E). Moreover,
162 R438W and A451V mutant mice had reduced number of Olig2+ oligodendrocytes in the
163 forebrain and midbrain compared to wild-type littermate mice (Fig. 2F). Olig2+ cells in
164 homozygous brain sections were consistently strongly reduced (>30%) compared to wild-type
165 mice, independent of age or sex. Of a combined 16 sets of littermate mice from both R438W and
166 A451V colonies, reduced neuronal or glial cell numbers were conspicuous in homozygous brain
167 sections of 12 littermate sets (Fig. 2E, F; see also Fig. 3), indicating incomplete penetrance of the
168 mutant phenotype. Collectively, these results suggest that Trabid's DUB and STRIPAK-binding
169 activities are required to produce the correct numbers of neuronal and glial cells in the
170 developing brain.
171
172 **Trabid mutant mice exhibit a motor deficit consistent with reduced numbers of**
173 **dopaminergic neurons and projections**
174 Given the cell number deficits in the midbrain of Trabid mutant mice and the reported midbrain
175 neurodegeneration and locomotor defects in Trabid mutant *Drosophila* (Kounatidis et al. 2017),
176 we asked if the numbers of dopaminergic neurons that control motor function might be affected
177 in Trabid R438W and A451V mutant mice. Midbrain and striatal coronal sections were
178 immunostained for Tyrosine Hydroxylase (TH), the rate-limiting enzyme for dopamine synthesis
179 and a marker of dopaminergic neurons. A reduction in the numbers of TH+ neurons was
180 observed in the substantia nigra pars compacta (SNc) of Trabid mutant mice from both R438W
181 and A451V colonies, independent of age or sex (Fig. 3A). SNc neurons project axons to the
182 striatum to produce an extensive network of axonal terminals that communicate with striatal
183 neurons (Matsuda et al. 2009). Consistent with the lack of prominent TH+ neuronal processes
184 emanating from the SNc neurons that remain in the mutant midbrain, TH immunoreactivity was
185 reduced in the striatum of homozygous R438W and A451V mutant mice (Fig. 3B, C). Also in

186 mutant brain sections, the reduced abundance and intensity of TH+ neuronal processes were
187 readily apparent in cortical regions including the motor cortex and claustrum that regulate motor
188 responses (Fig. 3B, C). Differences in TH staining in the mutant striatum compared to wild-type
189 were modest or not observed in all littermates examined (Fig. 3D), indicating incomplete
190 penetrance of the mutant Trabid alleles.
191
192 Given the altered abundance of TH+ cells and projections in motor-related brain regions of
193 Trabid mutant mice, we evaluated the motor function of these mice using a rotarod assay.
194 Homozygous R438W mice showed a significantly reduced latency to fall at 20, 25, 30 and 35
195 RPM, compared to controls (Fig. 3E), as did homozygous A451V animals at 30 and 35 RPM
196 (Fig. 3E). This indicates that Trabid patient mutations impair motor coordination, consistent with
197 a deficiency in dopaminergic neurons. The smaller size of R438W homozygous mice compared
198 to wild-type littermates (Fig. 2C) could be a contributing factor to the compromised rotarod
199 performance of these mutants. However, given that A451V homozygous mice on average are not
200 smaller than wild-type littermates, the motor deficit exhibited by both R438W and A451V
201 homozygous mice is likely caused by the abnormal cell numbers and reduced dopaminergic
202 neurons in their brains (Figs. 2 and 3). Taken together, these results suggest that Trabid regulates
203 the brain cellular architecture and neuronal circuitry required for normal motor function.
204
205 **Trabid patient mutants fail to efficiently limit APC ubiquitylation in cells**
206 To understand the molecular basis for the neuronal and behavioral phenotypes of Trabid mutant
207 mice, we focused on APC— an established regulator of mammalian brain development (Yokota
208 et al. 2009; Preitner et al. 2014) and a protein that we have shown becomes strongly
209 ubiquitylated upon loss of Trabid or Striatin (Tran et al. 2008; Tran et al. 2013). Moreover, given
210 that Striatin binds directly to APC (Breitman et al. 2008), we hypothesized that the Trabid
211 patient mutants impaired in DUB activity or Striatin-binding would impact APC ubiquitylation
212 and function in cells. To test this, we generated cells with doxycycline (dox)-inducible
213 expression of FLAG-Trabid and examined the ubiquitylation status of endogenous APC in dox-
214 treated cells. The levels of ubiquitin-modified APC were strongly suppressed in cells expressing
215 wild-type FLAG-Trabid (Fig. 4). In contrast, induction of the FLAG-Trabid R438W mutant, like
216 the catalytically dead FLAG-Trabid C443S, did not repress APC ubiquitylation, and induction of

217 FLAG-Trabid A451V expression only partially reduced APC ubiquitylation compared to control
218 cells (Fig. 4). These results suggest that both DUB and STRIPAK-binding activities of Trabid
219 are required for efficient deubiquitylation of APC in cells.
220
221 **Trabid patient mutants impede EGFP-APC transport to the leading edge of migrating cells**
222 APC decorates the membrane protrusions at the leading edge of migrating cells (Nathke et al.
223 1996) and we have shown that Trabid is a key regulator of APC localisation to these cortical
224 structures (Tran et al. 2013). Consistent with this insight, FLAG-Trabid localised prominently
225 with EGFP-APC in the tips of long cell processes (Fig. 5A). Analysis of several of these tip
226 clusters by super resolution microscopy revealed ~30% overlap between the FLAG-Trabid and
227 EGFP-APC signals, indicating that a significant fraction of these proteins co-localise in cortical
228 cell protrusions (Fig. 5B). In sub-confluent cultures, EGFP-APC localised strongly to the
229 lamellipodial leading edge of the majority of cells co-transfected wild-type FLAG-Trabid (Fig.
230 5C, D). By contrast, in cells transfected with the FLAG-Trabid mutants R438W and A451V,
231 EGFP-APC formed irregular puncta at sub-cortical regions close to the leading edge and EGFP-
232 APC aggregates are often sequestered to puncta formed by the R438W FLAG-Trabid mutant
233 (Fig. 5C, D). Such sites may contain ubiquitylated substrates bound to DUB-defective Trabid
234 mutants, as we have previously demonstrated with Trabid C443S (Tran et al. 2008; Licchesi et
235 al. 2012). Consistently, FLAG-Trabid C443S formed puncta that contained EGFP-APC near the
236 tips of long cell processes (Fig. 5E). The Trabid substrate HECTD1 was sequestered to C443S
237 puncta in the cytosol, but intriguingly not to puncta residing in proximity of the leading edge
238 membrane (Fig. 5E). In near-confluent cultures following prolonged co-transfection of FLAG-
239 Trabid mutants and EGFP-APC, we observed the striking phenomena of strong EGFP-APC
240 aggregation on or near the plasma membrane and thin tube-like processes extending between
241 neighbouring cells decorated with abundant EGFP-APC puncta/aggregates of various sizes (Fig.
242 5F). In cells co-transfected with wild-type FLAG-Trabid, EGFP-APC concentrated in cell tips
243 (Fig. 5F). Collectively, these results indicate that Trabid's DUB and STRIPAK-binding activities
244 are required for the efficient localisation of APC to plasma membrane sites involved in polarised
245 cell migration.
246

247 **Trabid patient mutations perturb the axonal trafficking of APC-tdTomato and impair the**
248 **trajectory of neurite outgrowth**
249 APC regulates the dynamic interactions of the microtubule and actin cytoskeletons at cortical
250 membranes to direct the formation of neuronal growth cones and the trajectory of axon growth
251 (Dogterom and Koenderink 2019). To investigate the effect of patient Trabid mutations on APC
252 localisation in primary neurons, we generated mice expressing an APC-tdTomato fluorescent
253 protein under the control of the endogenous *Apc* gene promoter (Fig. 6A). APC-tdTomato mice
254 were bred with knock-in mice carrying either the Trabid R438W or A451V mutant allele (Fig. 2)
255 and neural progenitors were isolated at embryonic day E11.5 from compound heterozygotes. We
256 then performed live cell imaging to analyse the trafficking of APC-tdTomato in neurites
257 extending from progenitors undergoing differentiation (Fig. 6A). Endogenous Trabid protein
258 levels were comparable in neural progenitor cultures derived from embryos bearing wild-type or
259 R438W and A451V mutant Trabid alleles (Fig. 6B). In neurons with wild-type Trabid, APC-
260 tdTomato accumulated strongly in the tips of growing neurites, marking prominent growth cones
261 that drive axon elongation (Fig. 6C; *Zranb1*$^{+/+}$). In neurons with heterozygous Trabid R438W or
262 A451V mutation, APC-tdTomato exhibited broad distribution along the length of the neurite and
263 the formation of growth cones were severely compromised (Fig. 6C, *Zranb1*$^{R438W/+}$). Tracking
264 analysis of the turn angles of APC-tdTomato intensities revealed that neurites with wild-type
265 Trabid elongated in a polarised manner, whereas neurites with R438W or A451V mutant Trabid
266 turned back or retracted at a greater frequency (Fig. 6D and E). These data suggest that Trabid's
267 DUB and STRIPAK-binding activities are required for efficient transport of APC to neurite tips
268 to promote the formation growth cones required for polarised axon elongation.
269
270
271 **Discussion**
272 We describe a novel function for the deubiquitylating enzyme Trabid as a key regulator of
273 axonal growth and guidance that likely underpins the neurodevelopmental defects observed in
274 children with Trabid mutation. Our data suggests that Trabid's mechanism of action is to
275 suppress the ubiquitylation of APC to regulate its intracellular trafficking. A *hypo*ubiquitylated
276 APC pool is efficiently localised to the cortical cytoskeleton where it directs neuronal growth
277 cone formation and polarised axon elongation. The identification of human Trabid variants that

278 disrupt the distribution of APC to the leading edge of migrating cells provides a plausible
279 explanation for the associated patient neuro-developmental disorders. Our work identifies
280 Trabid's DUB- and STRIPAK-binding activities, and the control of APC localisation, as crucial
281 events during embryonic and neural development.
282
283 The two patients carrying Trabid missense mutations R438W and A451V were diagnosed with a
284 range of distinct congenital disorders including craniofacial abnormalities, seizures,
285 developmental delay, autism—and both patients presented with microcephaly and constipation
286 (Deciphering Developmental Disorders 2015). We propose that the underlying cause of these
287 seemingly unrelated conditions, broadly classified as neurocristopathies, is the abnormal
288 specification or migration of neural crest cells in the developing embryo (Vega-Lopez et al.
289 2018). Discrete neural crest populations contribute to the development of craniofacial structures,
290 the forebrain and midbrain, and the enteric nervous system (Anderson et al. 2006; Creuzet et al.
291 2006). Therefore, errors in the formation or polarised migration of neural crest cells could
292 account for all the patient phenotypes, including the reduction in brain volume (microcephaly).
293 Presently, we can only speculate that the irregular cellular architecture and reduced cell numbers
294 in the brains of mice harbouring Trabid patient mutations (Figs. 2 and 3) reflect the errant
295 migration of neural crest or neural progenitor cell populations in early embryogenesis (Silva et
296 al. 2019). While Trabid mutant mice did not exhibit microcephaly, they showed a motor deficit
297 (Fig. 3) consistent with the locomotor defects reported for Trabid loss-of-function in *Drosophila*
298 (Kounatidis et al. 2017). Intriguingly, the fly Striatin homolog CKA is involved in axonal
299 transport and motor coordination (Neisch et al. 2017), and *Drosophila* Strip1 regulates
300 endosomal trafficking and axon elongation (Sakuma et al. 2014). Endosomal trafficking defects
301 have been linked to reduced proliferation of neural progenitors and microcephaly (Carpentieri et
302 al. 2022). Three independent groups have identified Trabid's association with STRIPAK (Sowa
303 et al. 2009; Tran et al. 2013; Harris et al. 2021). We have now established the functional
304 significance of this interaction. The requirement of Trabid binding to STRIPAK for efficient
305 protein trafficking, polarised axon growth, and motor coordination (Figs. 3, 5, 6), supports the
306 view that Trabid-STRIPAK regulates an evolutionarily conserved mechanism of cell movement
307 required for normal brain development and establishment of the correct neuronal circuitry in the
308 motor system.

309

310 The impairment of two distinct Trabid functions—polyubiquitin hydrolysis and STRIPAK-
311 binding—led to common cellular, developmental, and behavioral phenotypes (Figs. 2-6)
312 (Deciphering Developmental Disorders 2015), strongly suggesting that these activities act in the
313 same pathway. We propose that APC is the primary molecular target of Trabid action in
314 cytoskeleton organisation and polarised axon growth (Fig. 7). APC is an established regulator of
315 cell adhesion and migration, and it governs the cortical actin and microtubule cytoskeleton
316 dynamics required to form and steer axonal growth cones (Dogterom and Koenderink 2019;
317 Efimova et al. 2020). In a yeast two hybrid screen, we have found that Trabid and Striatin
318 interacted with the armadillo repeat domain (ARD) of APC, but not to an APC ARD mutant that
319 caused cell-cell adhesion defects (Hamada and Bienz 2002; Tran et al. 2008). This implies that a
320 functional interaction between Trabid, Striatin and APC promotes the fidelity of cell-cell or cell-
321 substratum contacts. Our model of Trabid action in Figure 7 integrates published data showing
322 that (1) Trabid complexes with Striatin/STRIPAK in human cell lines (Sowa et al. 2009; Tran et
323 al. 2013; Harris et al. 2021), and (2) Striatin binds directly to the ARD domain of APC (Breitman
324 et al. 2008). We propose that STRIPAK recruits Trabid to deubiquitylate APC. This allows APC
325 to accumulate at the leading edge of migrating cells to promote efficient, polarised locomotion
326 (Fig. 7A). The Trabid R438W mutant still binds STRIPAK and is recruited to APC, but it is
327 impaired in its ability to cleave ubiquitin chains from APC. And although the Trabid A451V
328 mutant retains full DUB activity, it cannot be recruited to APC via STRIPAK. Both mutant
329 scenarios cause APC to become persistently modified with ubiquitin chains that lead to APC
330 delocalisation from cell tips and defective cell movement (Fig. 7B). Consistent with this model,
331 Trabid and/or Striatin deficiency caused APC hyperubiquitylation and aggregation, perturbed
332 actin assembly and microtubule stability, and inhibited the migration of mouse and human cell
333 lines (Bai et al. 2011; Tran et al. 2013) (our unpublished data).
334

335 We have shown that ubiquitin-modified APC correlated with its binding to Axin in the β-catenin
336 destruction complex (Tran and Polakis 2012), whereas non-ubiquitin-modified APC accumulates
337 in membrane protrusions (Tran et al. 2013). Thus, reversible modification with polyubiquitin
338 could be the long-hypothesised molecular switch that regulates the distribution of APC between
339 its many functional pools in cells (Dikovskaya et al. 2001; Bienz 2002). Chronic APC

340 ubiquitylation in Trabid deficient/mutant cells might result in increased APC sequestration into
341 Axin destruction complexes or promote spurious interactions with ubiquitin binding proteins that
342 retard APC trafficking along microtubules. Rescue of the APC transport defect could
343 hypothetically be achieved by inhibition of glycogen synthase kinase 3 (GSK3), which we have
344 shown abolishes APC ubiquitylation (Tran and Polakis 2012). In support of this idea is the
345 finding that GSK3 inactivation promotes the association of APC with microtubule plus ends to
346 drive polarised cell migration (Etienne-Manneville and Hall 2003).
347
348 Optimal cell migration and adhesion requires stable, acetylated microtubules (Aguilar et al.
349 2014; Bance et al. 2019). Of note, loss of APC and the STRIPAK proteins STRIP1 and
350 CTTNBP2 strongly reduced the acetylated microtubule network in neurons (Yokota et al. 2009;
351 Shih et al. 2014; Sakuma et al. 2015). Furthermore, Striatin depletion perturbed cell-cell
352 adhesion (Breitman et al. 2008; Lahav-Ariel et al. 2019) and axon elongation defects caused by
353 STRIP1 mutation are linked to the dysregulation of neuronal adhesion (Sakuma et al. 2014). It
354 would be interesting to investigate if chronic APC ubiquitylation and dysfunction underlie all
355 Trabid and STRIPAK mutant phenotypes.
356
357
358 **Materials and Methods**
359 **Protein purification and characterisation**
360 Wild-type (WT), R438W, A451V, and C443S Trabid AnkOTU domains (245-697) were
361 expressed in BL21 competent *E. coli* and purified as described previously (Licchesi et al. 2012)
362 with minor modifications. *E. coli* cells were induced with 300 mM IPTG and grown overnight at
363 16°C. Cells were lysed by sonication in 50 mL lysis buffer (20 mM Tris pH 8.5, 200 mM NaCl,
364 10% glycerol, 1 mM PMSF, 2x Roche protease inhibitor tablets, 3 mM $MgCl_2$, 0.1 mg/mL
365 DNAse, 150 µL lysozyme, 10 mM β-mercaptoethanol) per 2 L culture. Anion-exchange
366 chromatography (MonoQ 5/50) was performed using the ÄKTA pure system at 4°C. See
367 Supplementary Figure 1 for the characterisation of the thermal stability and ubiquitin reactivity
368 of purified Trabid AnkOTU proteins. For DUB assays, a total of 20 µL reaction consisting of
369 0.25 µM purified AnkOTU domain was incubated with 1 µM of K29, K63 di-ubiquitin chains, or
370 K33-linked Tetra-Ub chains (R&D Systems) in DUB reaction buffer (50 mM NaCl, 50 mM Tris

371 pH 7.4, and 5 mM DTT) at 37°C. Reactions were stopped at the indicated times by addition of
372 SDS sample buffer and visualized by SDS-PAGE and silver staining (Silver Stain Plus; Biorad).
373
374 **Cells, plasmids, and antibodies**
375 An inducible lentiviral CRISPR/Cas9 system (Aubrey et al. 2015) was used to overexpress
376 Trabid in Figure 4. PCR amplified DNA encoding human wild-type or mutant Trabid with an N-
377 terminal FLAG tag was cloned into the EcoRI/NheI sites of a doxycycline-inducible pFTREtight
378 MCS rtTAadvanced puro lentiviral vector (Brumatti et al. 2013). Transduced HEK293 cells were
379 selected for puromycin resistance and pooled clones were used for experiments. Transient
380 transfection of plasmids pcDNA3.1-FLAG-Trabid (Tran et al. 2013), FLAG-Trabid mutants
381 generated by site-directed mutagenesis (QuikChange, Agilent), pEGFP-C1-APC (Rosin-
382 Arbesfeld et al. 2001), and pCMV-HA-HECTD1 (Sarkar and Zohn 2012) in HEK293T cells was
383 performed using Lipofectamine 2000 (Invitrogen). HEK293T cells (ATCC) and HEK293 cells
384 (Cellbank Australia) were authenticated by STR profiling and frequently tested for mycoplasma
385 contamination. Cells were cultured in DMEM supplemented with 10% FBS and 2 mM L-
386 Glutamine in a humidified incubator at 37°C with 5% CO_2. Mouse monoclonal Trabid antibodies
387 and rabbit polyclonal HectD1 antibodies have been described (Tran et al. 2013). Commercial
388 antibodies were purchased from a variety of vendors: anti-APC ALi 12-28 (Santa Cruz), anti-
389 Striatin (BD Biosciences), anti-Striatin3 (SG2NA, Novus Biologicals), anti-Strip1 (Abcepta)
390 anti-ubiquitin P4D1 (Cell Signaling), anti-FLAG M2, anti-β-actin-HRP AC-15, anti-β-tubulin
391 (Sigma), anti-HA 3F10 (Roche), anti-Tyrosine Hydroxylase (Millipore, AB152), anti-Ctip2
392 (Abcam, ab18465), and anti-Olig2 (Abcam, ab109186).
393
394 **Protein enrichment from cell lysates**
395 Confluent cells in 10 cm dishes were lysed on ice in 1 mL lysis buffer containing 1% IGEPAL
396 CA-630, 50 mM Tris-HCl, pH 7.5, 120 mM NaCl, 1 mM EDTA, and protease inhibitor tablets
397 (Roche). Lysates were centrifuged at 14,000 rpm for 10 min to remove cell debris. The
398 supernatant was assayed for protein (BCA kit, Pierce), then 1 mg total protein was
399 immunoprecipitated with anti-FLAG M2 antibody and protein G sepharose in a total volume of 1
400 mL lysis buffer. Enrichment of polyubiquitin chains was performed using purified GST-TUBE
401 (Tandem Ubiquitin Binding Entity) protein (Hjerpe et al. 2009). A volume of cell supernatant

402 containing 1 mg total protein was diluted 1:1 with 4M urea then incubated with 10 μg GST-
403 TUBE and Glutathione sepharose 4B. Immunoprecipitations and GST-TUBE pulldowns were
404 performed overnight with constant rotation at 4ºC. Protein complexes were washed twice with
405 lysis buffer and once with PBS, then eluted at 95ºC for 5 min in Laemmli buffer for Western
406 blotting analysis.
407
408 **Mice**
409 All mouse studies complied with relevant ethical regulations and were approved by the Walter
410 and Eliza Hall Institute Animal Ethics Committee. The *Zranb1*^{R438W}, *Zranb1*^{A451V}, and *Apc*^{tdTomato}
411 knock-in mice were generated on a C57BL/6J background using CRISPR–Cas9-mediated gene
412 editing by the Melbourne Advanced Genome Editing Centre (MAGEC) at the Walter and Eliza
413 Hall Institute. To generate a R438W mutation within the *Zranb1* gene on mouse chromosome 7,
414 a single guide (sg) RNA of the sequence GAC TAT ATG CAC TTT GGA AC was used to
415 create double stranded breaks within the Zranb1 locus to stimulate homologous recombination
416 and an oligo donor of the sequence TAT AAA CTG GTC TTT GGA GTT GGC TAC ACG TCT
417 GGA CAG TAG ACT ATA TGC ACT TTG GAA CTG GAC TGC CGG AGA TTG TTT ACT
418 TGA CTC AGT ACT ACA AGC TAC ATG GGG CAT TTA TGA CAA A was used to
419 introduce the R438W mutation. The sgRNA and donor sequence along with Cas9 mRNA were
420 injected into the cytoplasm of fertilized one-cell stage embryos generated from wild-type
421 C57BL/6J breeders. To generate the A451V mutation, a sgRNA of the sequence ACT CAG TAC
422 TAC AAG CTA CA and an oligo donor of the sequence ACA GTA GAC TAT ATG CAC TTT
423 GGA ACC GGA CTG CCG GAG ATT GTT TAC TTG ACT CAG TAC TAC AAG TCA CAT
424 GGG GCA TTT ATG ACA AAG ACT CGG TGC TTC GGA AAG CCC TGC ATG ACA GCC
425 TG CAT was used. Twenty-four hours later, two-cell stage embryos were transferred into the
426 uteri of pseudo-pregnant female mice. Viable offspring were genotyped by next-generation
427 sequencing. Targeted animals were backcrossed twice to wild-type C57BL/6J to eliminate off-
428 target mutations. Generation of C57BL/6J mice expressing the APC-tdTomato fusion protein
429 under the control of the endogenous *Apc* promoter (B6J.*Apc*^{tdTom}) were based on methods
430 previously described (Ng et al. 2020). Briefly, a sgRNA of the sequence AGA CGT CAC GAG
431 GTA AGA CC was used to create double stranded breaks within the *Apc* locus to stimulate
432 homologous recombination. A targeting vector containing homology arms of ~1.4 kilobases was

433 used to introduce the tdTomato coding sequence after the last *Apc* coding exon. Forward (ACC
434 TGT TCC TGT ACG GCA TG) and reverse (GCC TCC CAA AAT GAC CAG TG) primers to
435 detect the tdTomato sequence were used to screen viable pups for integration of the targeting
436 vector by PCR.
437
438 **Neurite outgrowth from cultured neural progenitors**
439 To generate mouse embryos expressing Apc-tdTomato with wild-type or mutant Trabid, mice
440 heterozygous for the Apc-tdTomato allele ($Apc^{tdTom/+}$) were outcrossed with mice heterozygous
441 for the Trabid R438W or A451V mutant allele ($Zranb1^{R438W/+}$ or $Zranb1^{A451V/+}$). Embryos at
442 E11.5 were harvested from pregnant females and ventral midbrains were dissected as previously
443 described (Thompson and Parish 2013). The isolated midbrain tissue was enzymatically
444 dissociated in Hank's Balanced Salt Solution containing 0.05% trypsin and 0.1% DNase I for 12
445 minutes at 37°C. Cells in the tissue were separated by mechanical dissociation, counted, then
446 plated in serum-free N2 medium consisting of a 1:1 mixture of Ham's F12 and Minimum
447 Essential Medium supplemented with 15 mM HEPES buffer, 1 mM glutamine, 6 mg/ml glucose,
448 1 mg/ml bovine serum albumin and N2 100X supplement. Cells were seeded at a density of
449 250,000 cells per well in a 24-well plate at 37°C, 3% CO_2. An aliquot of the resultant
450 neurosphere cultures were sequenced to ascertain genotypes. To differentiate midbrain
451 progenitors towards the dopaminergic lineage, neurospheres were resuspended in N2 medium
452 containing BDNF and GDNF (30 ng/ml each) then seeded in glass bottom ibidi chamber slides
453 pre-coated with poly-D-lysine and laminin (10 μg/ml each) for live imaging of neurite outgrowth
454 as described below.
455
456 **Histology and IHC analysis**
457 Mice were euthanized by CO_2 inhalation and intracardial perfusion was performed to fix the
458 tissues. Perfusion was initiated with Dulbecco's phosphate buffered saline followed by 10%
459 neutral buffered formalin (NBF). After perfusion, brain and tissues were dissected and post-fixed
460 in 10% NBF for 24h before paraffin-embedding with the Tissue-Tek VIP 6 automated tissue
461 processor (Sakura Finetek USA). Formalin-fixed paraffin-embedded tissues were sectioned
462 into 7 μm slices using a microtome and mounted on positively charged slides.
463 Immunohistochemistry (IHC) was performed with the Omnis Auto-immunostaining platform

464 using Agilent EnVision Target retrieval solution and the optimal dilution of the primary antibody
465 against the target protein. Secondary antibody detection was performed with the
466 Dako EnVision+ Single Reagents HRP and FLEX DAB+ Substrate Chromogen System. Slides
467 were counterstained with haematoxylin. Sections from wild-type, heterozygous and homozygous
468 littermate mice were mounted and stained on the same slide to ensure IHC signals can be directly
469 compared. Cell counts and IHC signal intensities were quantified using Fiji software (NIH). The
470 workflow for counting cells from IHC images is described in Supplementary Figure 2. IHC
471 signal intensities were measured as the optical density proportional to the concentration of the
472 stain. Briefly, the colour spectra of DAB- and haematoxylin-stained image was separated by
473 colour deconvolution, converted to greyscale, thresholding was applied, and the mean pixel
474 intensity of the region of interest was measured.
475
476 **Rotarod performance test**
477 The motor coordination of 3- to 4-month-old littermate mice from Trabid R438W and A451V
478 colonies were measured using a rotating rod (Rotamex-5, Columbus Instruments). Mice were
479 lowered onto a 3 cm diameter rod rotating at 12, 16, 20, 25, 30, 35, 40 or 45 revolutions per min
480 (RPM) for 2 min or until they fell. Animals were given a 5 min rest between RPM sessions. Two
481 trials were performed with a 1 h break between trials. The latency to fall was recorded for each
482 RPM. A 1 sec penalty was added if an animal failed to walk in time with the rod but rather
483 gripped the rod and rotated with it (cartwheel). Animals underwent 2 trials per day across 3 days.
484
485 **Microscopy and image analysis**
486 *Confocal microscopy* – Cells grown in Lab-Tek II chamber slides were fixed with 4%
487 paraformaldehyde for 10 min at room temperature, then permeabilized with 0.2% Triton-X100
488 and blocked with 5% normal goat serum (NGS). Cells were incubated with primary antibodies
489 diluted in 5% NGS overnight at 4ºC, followed by Alexa Fluor-conjugated secondary antibodies
490 for 1h at room temperature. ProLong Gold antifade reagent with DAPI was used to mount
491 coverslips to microscope slides. Confocal images were acquired on a Zeiss LSM 880 Airyscan
492 microscope using a 63x/1.4 N.A. oil objective, and 405, 488 and 594nm lasers. Maximum
493 intensity projections of raw images comprising 10-15 *z* sections were created using Fiji.
494

495 *3D structured illumination microscopy* – Super-resolution three-dimensional structured
496 illumination microscopy (3D-SIM) was performed on the DeltaVision OMX-SR system using
497 a 60x/1.42 N.A. PlanApo oil immersion objective, sCMOS cameras, and 488, 568 and 640 nm
498 lasers. 3D-SIM images consisted of 15 raw images per focal plane per colour channel with 125
499 nm between each z-step. Images were reconstructed and the colour channels aligned using the
500 reconstruction and alignment algorithms in softWoRx 7.0. Fraction of overlap between FLAG-
501 Trabid and EGFP-APC were measured in Imaris 9.2.
502
503 *Lattice lightsheet time-lapse imaging and analysis* – Live cell time-lapse imaging of APC-
504 tdTomato fluorescence in growing neurites was acquired using the Zeiss Lattice Light Sheet 7
505 microscope. A 561 nm laser formed a light sheet of length 30 µm with a thickness of 1 µm at the
506 sample plane via a 13.3 x, 0.44 NA objective. tdTomato fluorescence was collected via a 44.83
507 X, 1 NA detection objective lens. Data was collected with a frame rate of 60 ms and a z-step of
508 300 nm. Each region was imaged at 15-min intervals for 4-6 hours. Fluorescence was collected
509 via a multi-band stop, LBF 405/488/561/633, filter. Images were subsequently deskewed using
510 Zeiss's Zen 3.4 software. Samples were measured at 37°C and 5% CO_2. Maximum intensity
511 projections were created from the deskewed data in Fiji. Neurite tips were tracked using
512 Trackmate (v6.0.3) and LoG detector with 12 µm diameter, 0.08 threshold, no filters, and
513 subpixel localisation turned on. A minimum of 5 frames were set for track inclusion. Turn angles
514 were calculated using Matlab R2019b. Three points were used to calculate the turn. The first two
515 points determine the direction of neurite growth. The angle between this direction to the third
516 point determines the turn angle of the neurite. The turn angle was normalized such that 0º
517 constitutes a step straight forward with no turn and 180º is a turn backwards.
518
519
520 **Acknowledgements**
521 We are indebted to Prof David L. Vaux for his generous support and mentorship in the early
522 stages of this study. We thank Drs S. Wilcox, S. Scutts, J. Heath, D. Newgreen, J. Vince, C.
523 Parish, K. Scicluna, M. Herold, V. Wimmer, T. Thomas, K. Newton and V. Dixit for discussion,
524 reagents and technical support; and WEHI's Bioservices staff for outstanding animal care. Part
525 of the funding for this study was provided by the Australian National Health and Medical

Research Council (Ideas Grant #1181580 to E.V., H.T., and B.M.T). G.D. was supported by a fellowship from the Bodhi Education Fund. Work in the authors' laboratory is made possible by operational infrastructure grants through the Australian Government Independent Research Institutes Infrastructure Support (IRISS) and the Victorian State Government OIS. The generation of all mutant and transgenic mice used in this study was supported by Phenomics Australia and the Australian Government through the National Collaborative Research Infrastructure Strategy (NCRIS) program.

Author Contributions

D.F. designed and performed the protein biochemistry experiments, quantified cell numbers from histological sections, and assisted with the generation and maintenance of neurosphere cultures. M.B. designed and performed the rotarod experiments and assisted with analysis of the rotarod and histology data. M.M. performed 3D-SIM microscopy, live cell imaging of Apc-tdTomato trafficking, and analysed the data. A.K. designed the targeting vectors for generation of knock-in mice. E.T. assisted with the design of histology experiments. C.H. performed the genotyping. G.K. assisted with statistical analysis of the rotarod data and quantified IHC intensities. A.V., C.M., M.F., K.R., B.T., and E.V. analysed data. D.K. analysed data and provided study feedback and advice. G.D. supervised the study, analysed and conceptualized data, and edited the manuscript. H.T. conceived the project, designed, performed and supervised experiments, analysed and conceptualized data, and wrote the manuscript. All authors have read and commented on the manuscript.

Competing Interest Statement

D.K. is founder, shareholder and serves on the SAB of Entact Bio.

556 **References**

557 Aguilar A, Becker L, Tedeschi T, Heller S, Iomini C, Nachury MV. 2014. Alpha-tubulin K40
558 acetylation is required for contact inhibition of proliferation and cell-substrate adhesion.
559 *Mol Biol Cell* **25**: 1854-1866.

560 Anderson RB, Newgreen DF, Young HM. 2006. Neural crest and the development of the enteric
561 nervous system. *Adv Exp Med Biol* **589**: 181-196.

562 Aubrey BJ, Kelly GL, Kueh AJ, Brennan MS, O'Connor L, Milla L, Wilcox S, Tai L, Strasser A,
563 Herold MJ. 2015. An inducible lentiviral guide RNA platform enables the identification of
564 tumor-essential genes and tumor-promoting mutations in vivo. *Cell Rep* **10**: 1422-1432.

565 Bai SW, Herrera-Abreu MT, Rohn JL, Racine V, Tajadura V, Suryavanshi N, Bechtel S, Wiemann
566 S, Baum B, Ridley AJ. 2011. Identification and characterization of a set of conserved and
567 new regulators of cytoskeletal organization, cell morphology and migration. *BMC Biol* **9**:
568 54.

569 Bance B, Seetharaman S, Leduc C, Boeda B, Etienne-Manneville S. 2019. Microtubule acetylation
570 but not detyrosination promotes focal adhesion dynamics and astrocyte migration. *J Cell*
571 *Sci* **132**.

572 Bazzi H, Soroka E, Alcorn HL, Anderson KV. 2017. STRIP1, a core component of STRIPAK
573 complexes, is essential for normal mesoderm migration in the mouse embryo. *Proc Natl*
574 *Acad Sci U S A* **114**: E10928-E10936.

575 Beck DB, Basar MA, Asmar AJ, Thompson JJ, Oda H, Uehara DT, Saida K, Pajusalu S, Talvik I,
576 D'Souza P et al. 2021. Linkage-specific deubiquitylation by OTUD5 defines an embryonic
577 pathway intolerant to genomic variation. *Sci Adv* **7**.

578 Bienz M. 2002. The subcellular destinations of APC proteins. *Nat Rev Mol Cell Biol* **3**: 328-338.

579 Blanpain C, Lowry WE, Geoghegan A, Polak L, Fuchs E. 2004. Self-renewal, multipotency, and
580 the existence of two cell populations within an epithelial stem cell niche. *Cell* **118**: 635-
581 648.

582 Breitman M, Zilberberg A, Caspi M, Rosin-Arbesfeld R. 2008. The armadillo repeat domain of
583 the APC tumor suppressor protein interacts with Striatin family members. *Biochim Biophys*
584 *Acta* **1783**: 1792-1802.

585 Brumatti G, Salmanidis M, Kok CH, Bilardi RA, Sandow JJ, Silke N, Mason K, Visser J, Jabbour
586 AM, Glaser SP et al. 2013. HoxA9 regulated Bcl-2 expression mediates survival of

587 myeloid progenitors and the severity of HoxA9-dependent leukemia. *Oncotarget* **4**: 1933-
588 1947.
589 Carpentieri JA, Di Cicco A, Lampic M, Andreau D, Del Maestro L, El Marjou F, Coquand L,
590 Bahi-Buisson N, Brault JB, Baffet AD. 2022. Endosomal trafficking defects alter neural
591 progenitor proliferation and cause microcephaly. *Nat Commun* **13**: 16.
592 Castets F, Rakitina T, Gaillard S, Moqrich A, Mattei MG, Monneron A. 2000. Zinedin, SG2NA,
593 and striatin are calmodulin-binding, WD repeat proteins principally expressed in the brain.
594 *J Biol Chem* **275**: 19970-19977.
595 Chen YH, Huang TY, Lin YT, Lin SY, Li WH, Hsiao HJ, Yan RL, Tang HW, Shen ZQ, Chen GC
596 et al. 2021. VPS34 K29/K48 branched ubiquitination governed by UBE3C and TRABID
597 regulates autophagy, proteostasis and liver metabolism. *Nat Commun* **12**: 1322.
598 Clague MJ, Urbe S, Komander D. 2019. Breaking the chains: deubiquitylating enzyme specificity
599 begets function. *Nat Rev Mol Cell Biol*.
600 Creuzet SE, Martinez S, Le Douarin NM. 2006. The cephalic neural crest exerts a critical effect
601 on forebrain and midbrain development. *Proc Natl Acad Sci U S A* **103**: 14033-14038.
602 Deciphering Developmental Disorders S. 2015. Large-scale discovery of novel genetic causes of
603 developmental disorders. *Nature* **519**: 223-228.
604 Dickinson ME, Flenniken AM, Ji X, Teboul L, Wong MD, White JK, Meehan TF, Weninger WJ,
605 Westerberg H, Adissu H et al. 2016. High-throughput discovery of novel developmental
606 phenotypes. *Nature* **537**: 508-514.
607 Dikovskaya D, Zumbrunn J, Penman GA, Nathke IS. 2001. The adenomatous polyposis coli
608 protein: in the limelight out at the edge. *Trends Cell Biol* **11**: 378-384.
609 Dogterom M, Koenderink GH. 2019. Actin-microtubule crosstalk in cell biology. *Nat Rev Mol*
610 *Cell Biol* **20**: 38-54.
611 Efimova N, Yang C, Chia JX, Li N, Lengner CJ, Neufeld KL, Svitkina TM. 2020. Branched actin
612 networks are assembled on microtubules by adenomatous polyposis coli for targeted
613 membrane protrusion. *J Cell Biol* **219**.
614 Erpapazoglou Z, Walker O, Haguenauer-Tsapis R. 2014. Versatile roles of k63-linked ubiquitin
615 chains in trafficking. *Cells* **3**: 1027-1088.
616 Etienne-Manneville S, Hall A. 2003. Cdc42 regulates GSK-3beta and adenomatous polyposis coli
617 to control cell polarity. *Nature* **421**: 753-756.

618 Hamada F, Bienz M. 2002. A Drosophila APC tumour suppressor homologue functions in cellular
619 adhesion. *Nat Cell Biol* **4**: 208-213.
620 Harris LD, Le Pen J, Scholz N, Mieszczanek J, Vaughan N, Davis S, Berridge G, Kessler BM,
621 Bienz M, Licchesi JDF. 2021. The deubiquitinase TRABID stabilizes the K29/K48-
622 specific E3 ubiquitin ligase HECTD1. *J Biol Chem* **296**: 100246.
623 Hjerpe R, Aillet F, Lopitz-Otsoa F, Lang V, England P, Rodriguez MS. 2009. Efficient protection
624 and isolation of ubiquitylated proteins using tandem ubiquitin-binding entities. *EMBO Rep*
625 **10**: 1250-1258.
626 Hwang J, Pallas DC. 2014. STRIPAK complexes: structure, biological function, and involvement
627 in human diseases. *Int J Biochem Cell Biol* **47**: 118-148.
628 Komander D, Clague MJ, Urbe S. 2009. Breaking the chains: structure and function of the
629 deubiquitinases. *Nat Rev Mol Cell Biol* **10**: 550-563.
630 Kounatidis I, Chtarbanova S, Cao Y, Hayne M, Jayanth D, Ganetzky B, Ligoxygakis P. 2017. NF-
631 kappaB Immunity in the Brain Determines Fly Lifespan in Healthy Aging and Age-Related
632 Neurodegeneration. *Cell Rep* **19**: 836-848.
633 Kristariyanto YA, Abdul Rehman SA, Campbell DG, Morrice NA, Johnson C, Toth R, Kulathu
634 Y. 2015. K29-selective ubiquitin binding domain reveals structural basis of specificity and
635 heterotypic nature of k29 polyubiquitin. *Mol Cell* **58**: 83-94.
636 Kuck U, Radchenko D, Teichert I. 2019. STRIPAK, a highly conserved signaling complex,
637 controls multiple eukaryotic cellular and developmental processes and is linked with
638 human diseases. *Biol Chem* **400**: 1005-1022.
639 Lahav-Ariel L, Caspi M, Nadar-Ponniah PT, Zelikson N, Hofmann I, Hanson KK, Franke WW,
640 Sklan EH, Avraham KB, Rosin-Arbesfeld R. 2019. Striatin is a novel modulator of cell
641 adhesion. *FASEB J* **33**: 4729-4740.
642 Leto DE, Morgens DW, Zhang L, Walczak CP, Elias JE, Bassik MC, Kopito RR. 2019. Genome-
643 wide CRISPR Analysis Identifies Substrate-Specific Conjugation Modules in ER-
644 Associated Degradation. *Mol Cell* **73**: 377-389 e311.
645 Licchesi JD, Mieszczanek J, Mevissen TE, Rutherford TJ, Akutsu M, Virdee S, El Oualid F, Chin
646 JW, Ovaa H, Bienz M et al. 2012. An ankyrin-repeat ubiquitin-binding domain determines
647 TRABID's specificity for atypical ubiquitin chains. *Nature structural & molecular biology*
648 **19**: 62-71.

649 Madsen CD, Hooper S, Tozluoglu M, Bruckbauer A, Fletcher G, Erler JT, Bates PA, Thompson
650 B, Sahai E. 2015. STRIPAK components determine mode of cancer cell migration and
651 metastasis. *Nat Cell Biol* **17**: 68-80.
652 Matsuda W, Furuta T, Nakamura KC, Hioki H, Fujiyama F, Arai R, Kaneko T. 2009. Single
653 nigrostriatal dopaminergic neurons form widely spread and highly dense axonal
654 arborizations in the neostriatum. *J Neurosci* **29**: 444-453.
655 Nathke IS, Adams CL, Polakis P, Sellin JH, Nelson WJ. 1996. The adenomatous polyposis coli
656 tumor suppressor protein localizes to plasma membrane sites involved in active cell
657 migration. *J Cell Biol* **134**: 165-179.
658 Neisch AL, Neufeld TP, Hays TS. 2017. A STRIPAK complex mediates axonal transport of
659 autophagosomes and dense core vesicles through PP2A regulation. *J Cell Biol* **216**: 441-
660 461.
661 Ng SS, De Labastida Rivera F, Yan J, Corvino D, Das I, Zhang P, Kuns R, Chauhan SB, Hou J,
662 Li XY et al. 2020. The NK cell granule protein NKG7 regulates cytotoxic granule
663 exocytosis and inflammation. *Nat Immunol* **21**: 1205-1218.
664 Preitner N, Quan J, Nowakowski DW, Hancock ML, Shi J, Tcherkezian J, Young-Pearse TL,
665 Flanagan JG. 2014. APC is an RNA-binding protein, and its interactome provides a link to
666 neural development and microtubule assembly. *Cell* **158**: 368-382.
667 Rosin-Arbesfeld R, Ihrke G, Bienz M. 2001. Actin-dependent membrane association of the APC
668 tumour suppressor in polarized mammalian epithelial cells. *EMBO J* **20**: 5929-5939.
669 Sakuma C, Kawauchi T, Haraguchi S, Shikanai M, Yamaguchi Y, Gelfand VI, Luo L, Miura M,
670 Chihara T. 2014. Drosophila Strip serves as a platform for early endosome organization
671 during axon elongation. *Nat Commun* **5**: 5180.
672 Sakuma C, Okumura M, Umehara T, Miura M, Chihara T. 2015. A STRIPAK component Strip
673 regulates neuronal morphogenesis by affecting microtubule stability. *Sci Rep* **5**: 17769.
674 Sarkar AA, Zohn IE. 2012. Hectd1 regulates intracellular localization and secretion of Hsp90 to
675 control cellular behavior of the cranial mesenchyme. *J Cell Biol* **196**: 789-800.
676 Shih PY, Lee SP, Chen YK, Hsueh YP. 2014. Cortactin-binding protein 2 increases microtubule
677 stability and regulates dendritic arborization. *J Cell Sci* **127**: 3521-3534.
678 Silva CG, Peyre E, Nguyen L. 2019. Cell migration promotes dynamic cellular interactions to
679 control cerebral cortex morphogenesis. *Nat Rev Neurosci* **20**: 318-329.

680 Sowa ME, Bennett EJ, Gygi SP, Harper JW. 2009. Defining the human deubiquitinating enzyme
681 interaction landscape. *Cell* **138**: 389-403.
682 Thompson LH, Parish CL. 2013. Transplantation of fetal midbrain dopamine progenitors into a
683 rodent model of Parkinson's disease. *Methods Mol Biol* **1059**: 169-180.
684 Tran H, Bustos D, Yeh R, Rubinfeld B, Lam C, Shriver S, Zilberleyb I, Lee MW, Phu L, Sarkar
685 AA et al. 2013. HectD1 E3 ligase modifies adenomatous polyposis coli (APC) with
686 polyubiquitin to promote the APC-axin interaction. *J Biol Chem* **288**: 3753-3767.
687 Tran H, Hamada F, Schwarz-Romond T, Bienz M. 2008. Trabid, a new positive regulator of Wnt-
688 induced transcription with preference for binding and cleaving K63-linked ubiquitin
689 chains. *Genes Dev* **22**: 528-542.
690 Tran H, Polakis P. 2012. Reversible modification of adenomatous polyposis coli (APC) with K63-
691 linked polyubiquitin regulates the assembly and activity of the beta-catenin destruction
692 complex. *J Biol Chem* **287**: 28552-28563.
693 Vaughan N, Scholz N, Lindon C, Licchesi JDF. 2022. The E3 ubiquitin ligase HECTD1
694 contributes to cell proliferation through an effect on mitosis. *Sci Rep* **12**: 13160.
695 Vega-Lopez GA, Cerrizuela S, Tribulo C, Aybar MJ. 2018. Neurocristopathies: New insights 150
696 years after the neural crest discovery. *Dev Biol* **444 Suppl 1**: S110-S143.
697 Yokota Y, Kim WY, Chen Y, Wang X, Stanco A, Komuro Y, Snider W, Anton ES. 2009. The
698 adenomatous polyposis coli protein is an essential regulator of radial glial polarity and
699 construction of the cerebral cortex. *Neuron* **61**: 42-56.
700 Yu Y, Zheng Q, Erramilli SK, Pan M, Park S, Xie Y, Li J, Fei J, Kossiakoff AA, Liu L et al. 2021.
701 K29-linked ubiquitin signaling regulates proteotoxic stress response and cell cycle. *Nat*
702 *Chem Biol* **17**: 896-905.
703 Yuan WC, Lee YR, Lin SY, Chang LY, Tan YP, Hung CC, Kuo JC, Liu CH, Lin MY, Xu M et
704 al. 2014. K33-Linked Polyubiquitination of Coronin 7 by Cul3-KLHL20 Ubiquitin E3
705 Ligase Regulates Protein Trafficking. *Mol Cell* **54**: 586-600.
706

707 **Figures**

Figure 1

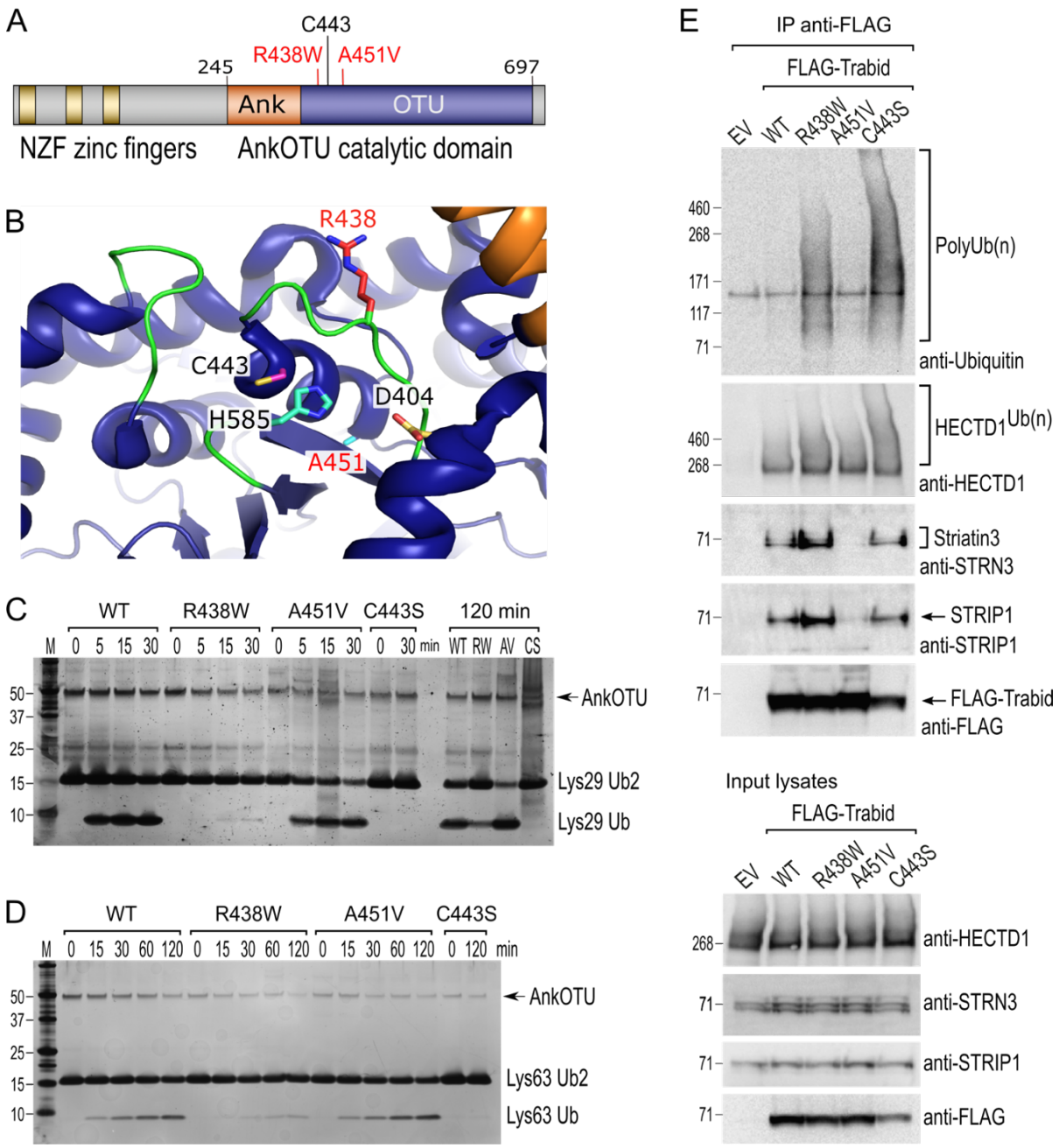

708

709 **Figure 1. Trabid patient mutants are impaired in DUB activity and STRIPAK binding.**

710 **A**. Trabid patient mutations R438W and A451V flank either side of the catalytic cysteine C443

711 in Trabid's AnkOTU domain.

712 **B**. Residue R438 project prominently into the catalytic cleft formed by the Ank and OTU
713 domain, whereas residue A451 reside at the back of the active site. The positions of the catalytic
714 triad residues C443, H585 and D404 are shown. Crystal structure of AnkOTU domain: PDB
715 3ZRH.
716 **C** and **D**. *In vitro* DUB assays. Hydrolysis of Lys29-linked (C) and Lys63-linked (D) di-
717 ubiquitin chains by purified wild-type and mutant Trabid AnkOTU proteins. The Trabid R438W
718 AnkOTU domain exhibit strongly reduced DUB activity M, molecular weight markers in
719 kilodaltons.
720 **E**. Immunoprecipitation of FLAG-Trabid from the lysates of transfected HEK293T cells showed
721 that FLAG-Trabid R438W and C443S mutants co-precipitated high amounts of endogenous
722 polyubiquitin (PolyUb(n) smear), indicating impaired DUB activity. FLAG-Trabid A451V failed
723 to efficiently co-precipitate Striatin3 and STRIP1, indicating loss of binding to the STRIPAK
724 complex. All FLAG-Trabid proteins co-precipitated similar amounts of the E3 ubiquitin ligase
725 HECTD1. EV, empty vector control.
726
727
728
729
730
731
732
733
734
735
736
737
738
739

Figure 2

A

Knock-in mouse models

Zranb1$^{R438W/+}$ and *Zranb1*$^{A451V/+}$ (KI/+)

Zranb1$^{R438W/R438W}$ and *Zranb1*$^{A451V/A451V}$ (KI/KI)

B

Observed number of mice of all genotypes

	+/+	KI/+	KI/KI
R438W colony (n=184)	59	89	36
Expected Mendelian 1:2:1 ratio	46	92	46
A451V colony (n=220)	50	101	69
Expected Mendelian 1:2:1 ratio	55	110	55

C

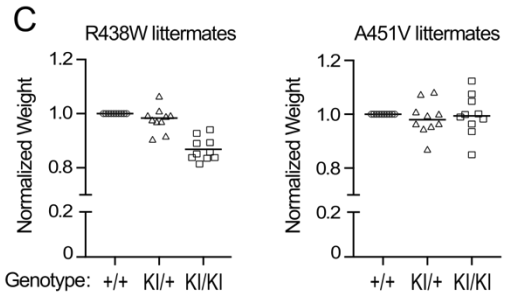

D

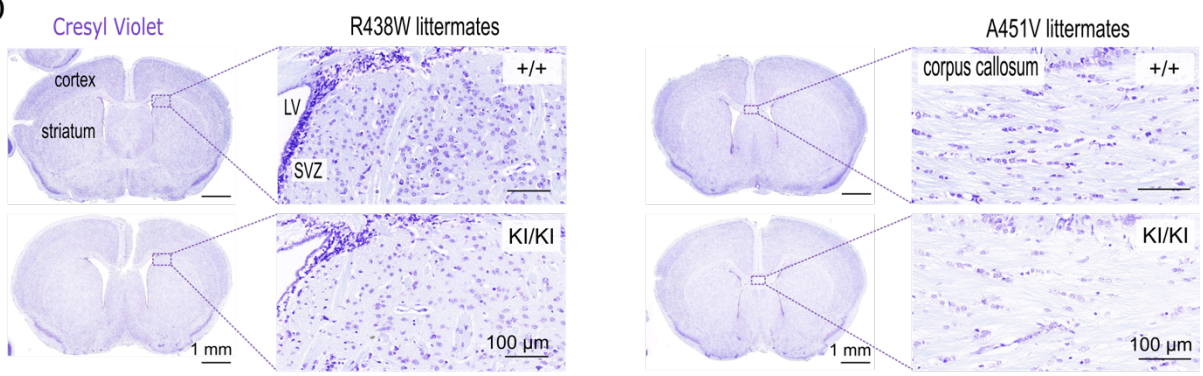

E

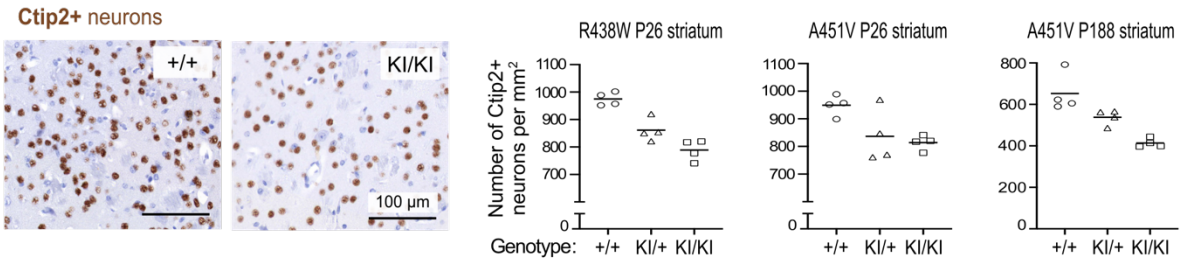

F

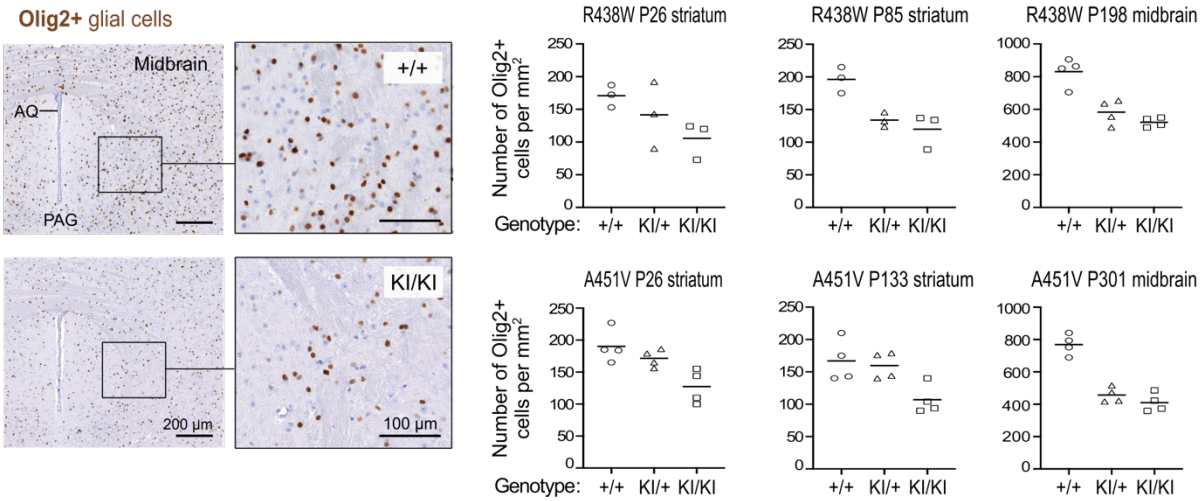

740

741 **Figure 2. Decreased cell density in the brains of mice harbouring Trabid patient mutations.**
742 **A**. Schematic of knock-in mouse strains harbouring *Zranb1/Trabid* patient mutations generated
743 by CRISPR/Cas9 genome editing.
744 **B**. Numbers of mice of all genotypes produced from heterozygous intercrosses in the R438W or
745 A451V colony, respectively.
746 **C**. Normalized weight of 10 sets of weaned littermate mice (5 males, 5 females; age range P26-
747 P222) from each Trabid mutant colony. For each set of littermates, the weight of the wild-type
748 (+/+) mouse was set at 1 and the weight of KI/+ or KI/KI mutant mice expressed as a ratio of the
749 wild-type mouse weight.
750 **D**. Coronal brain sections (Bregma ±0.3mm) of weaned (postnatal day P26) littermate males
751 from the R438W and A451V mouse colonies were stained with Cresyl Violet to assess general
752 anatomy and cellular organisation in the cerebral cortex and striatum. LV, lateral ventricle; SVZ,
753 subventricular zone. An overall decrease in Cresyl Violet staining intensity was evident in
754 mutant homozygous (KI/KI) sections from both mouse strains compared to similar sections from
755 the respective wild-type (+/+) littermate.
756 **E**. Ctip2 IHC revealed reduced numbers of medium spiny neurons in the striatum of mutant mice
757 from the R438W and A451V colonies compared to wild-type littermate mice. Representative
758 images shown are coronal brain sections of P26 male littermates from the R438W colony. Each
759 data point represents the cell count in a randomly selected, non-overlapping 1 mm square area in
760 the striatum from both brain hemispheres. The age and brain region of the cell count for 3 sets of
761 littermate mice from the indicated mutant strain are specified. Cell numbers were quantified
762 blinded to genotype using images processed in Fiji software. See Supplementary Figure 2.
763 **F.** Olig2 IHC revealed reduced numbers of oligodendrocytes in the striatum and midbrain of
764 homozygous mice from the R438W and A451V colonies compared to respective wild-type
765 littermates. Representative images shown are coronal sections from the ventral midbrain of P301
766 female littermates from the A451V colony (AQ, cerebral aqueduct; PAQ, periaqueductal gray).
767 Each data point represents the cell count in a randomly selected, non-overlapping 1 mm square
768 area in the striatum or midbrain from both brain hemispheres. The age and brain region of the
769 cell count for 3 sets of littermate mice from the indicated mutant strain are specified. Cell
770 numbers were quantified blinded to genotype using images processed in Fiji. See Supplementary
771 Figure 2.

Figure 3

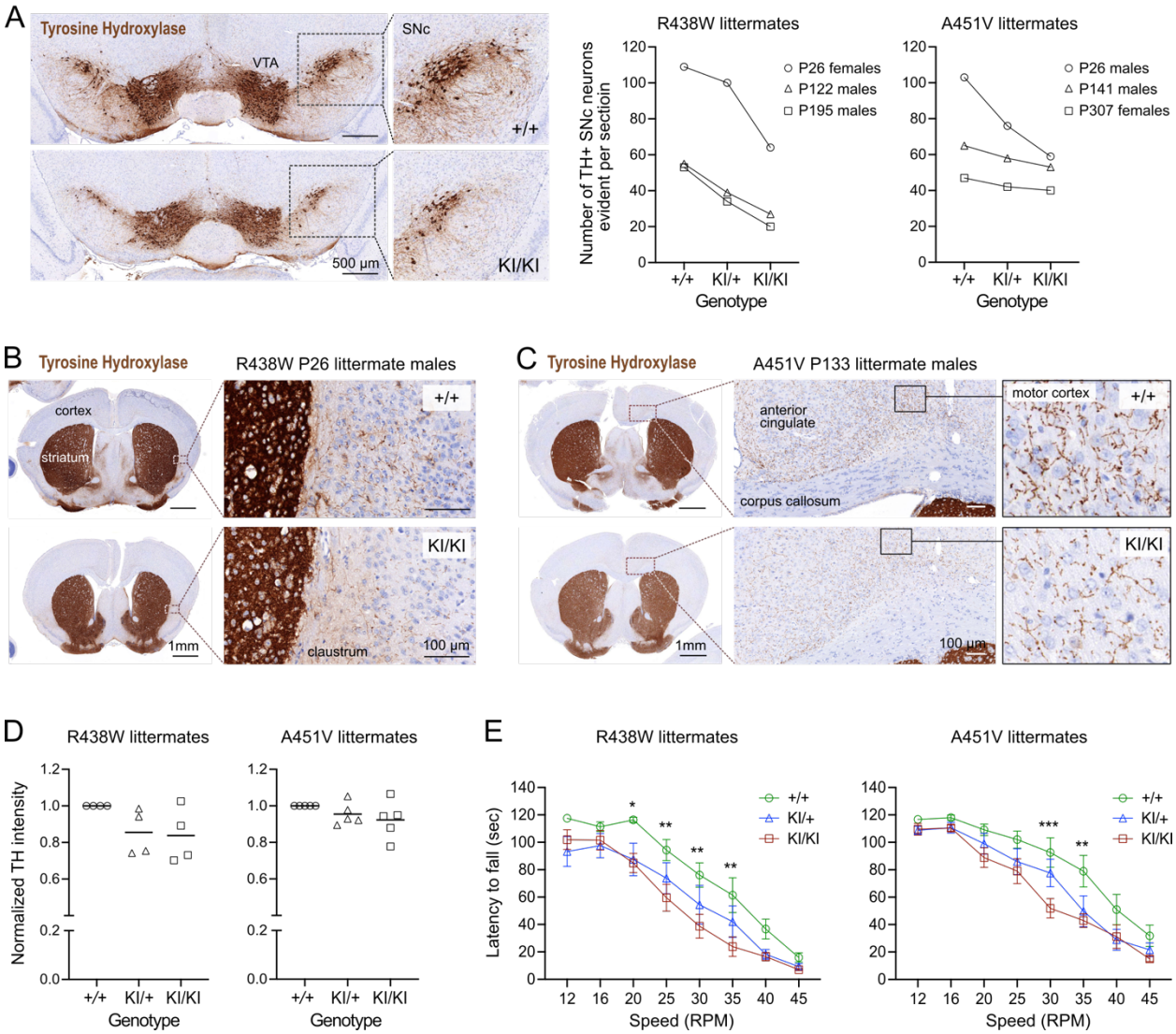

Figure 3. Trabid mutant mice exhibit a motor deficit consistent with reduced numbers of dopaminergic neurons and projections.

A. Tyrosine Hydroxylase (TH) IHC of coronal midbrain sections revealed reduced numbers of TH+ dopaminergic neurons in the substantia nigra pars compacta (SNc) of homozygous mutant mice from the Trabid R438W and A451V colonies compared to similar midbrain sections of the respective wild-type littermates. Representative images shown are midbrain sections of P26 female littermates from the R438W colony. VTA, ventral tegmental area. Numbers of TH+ SNc neurons were quantified using IHC images processed in Fiji. See Supplementary Figure 2.

782 **B**. Tyrosine Hydroxylase IHC of coronal brain sections (Bregma ±0.3mm) of P26 littermate
783 mice from the Trabid R438W colony revealed reduced TH staining intensity in the striatum and
784 fewer TH+ projections in the adjacent cortex of homozygous mutant mice compared to similar
785 regions in the wild-type littermate (magnified area).
786 **C**. Tyrosine Hydroxylase IHC of coronal brain sections (Bregma ±0.3mm) of P133 littermate
787 mice from the Trabid A451V colony revealed reduced abundance and intensity of TH+
788 projections in several cortical regions including the primary/secondary motor cortex of
789 homozygous mutant mice compared to similar regions in the wild-type littermate (magnified
790 area).
791 **D**. Tyrosine Hydroxylase staining intensity in the striatum of mutant mice from the R438W and
792 A451V colonies normalized to the staining intensity of wild-type littermate sections. IHC signals
793 were measured as the optical density of the region of interest demarcated manually using Fiji.
794 Each symbol represents one mouse of the indicated genotype belonging to a set of littermate
795 mice from the R438W colony (n=4 sets: P26 males, P93 females, P307 males, P480 females) or
796 the A451V colony (n=5 sets: P26 males, P41 females, P133 males, P188 females, P303 females).
797 **E**. Rotarod performance of 3 to 4-month-old littermate mice from the R438W and A451V
798 colonies. Each data point represents the average latencies of 8 mice (4 males, 4 females), where
799 each mouse was subjected to 6 trials over 3 days. Wild-type (+/+), heterozygous (KI/+) and
800 homozygous (KI/KI) littermate mice were tested together. The experimenter was blinded to
801 genotype. A repeated measures two-way ANOVA and Dunnett's multiple comparisons test was
802 applied to the data, using wild-type mice as the control group. Asterisks denote statistically
803 significant differences between wild-type (+/+) and homozygous (KI/KI) mutant mice. *$p<0.05$,
804 **$p<0.01$, ***$p<0.001$. Error bars, ±SEM.
805
806
807
808
809
810
811

Figure 4

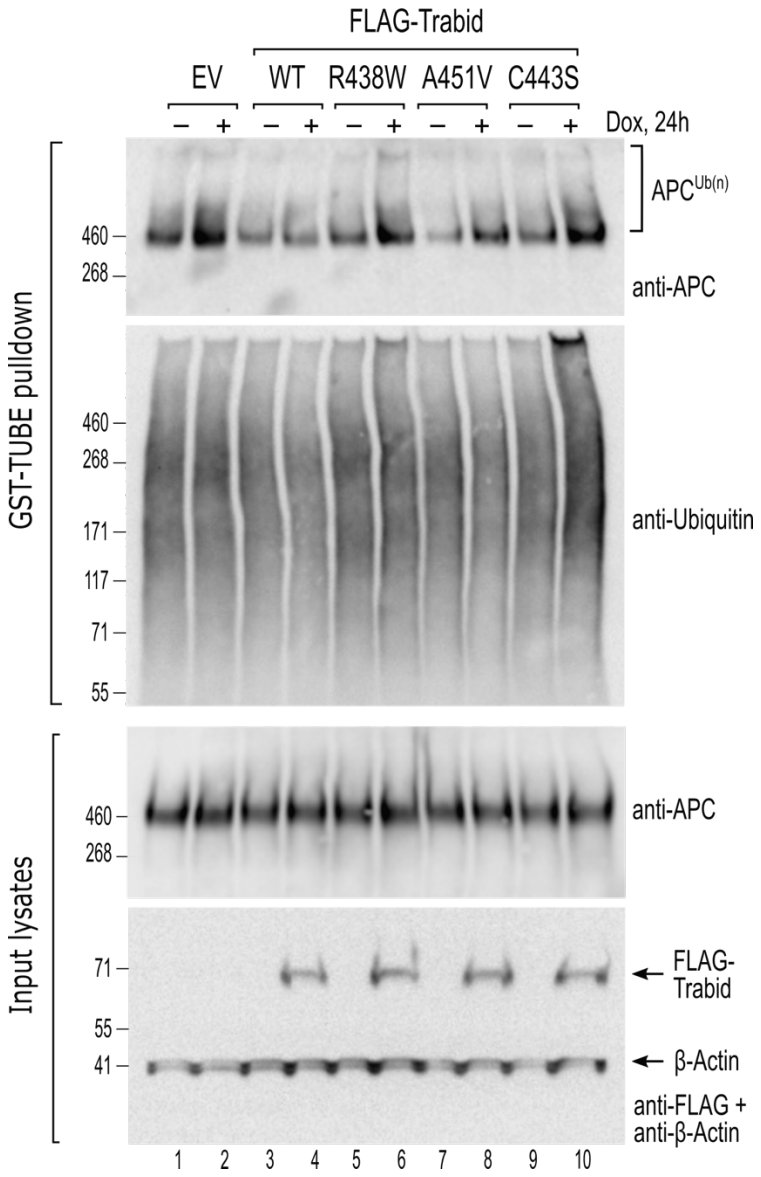

Figure 4. Trabid patient mutants fail to efficiently suppress APC ubiquitylation in cells. HEK293 cells stably transfected with doxycycline inducible constructs for the expression of wild-type or mutant FLAG-Trabid were untreated (-) or treated with dox (+; 100 ng/ml) for 24h. Cell lysates were subjected to a GST-TUBE pulldown to enrich the ubiquitylated proteome. Precipitated material and input lysates were processed for Western blotting using the indicated antibodies. Endogenous APC protein levels remained unchanged irrespective of FLAG-Trabid expression (input lysates), but ubiquitylated APC species were only efficiently suppressed by wild-type FLAG-Trabid expression ($APC^{Ub(n)}$; WT +). EV, empty vector control.

Figure 5

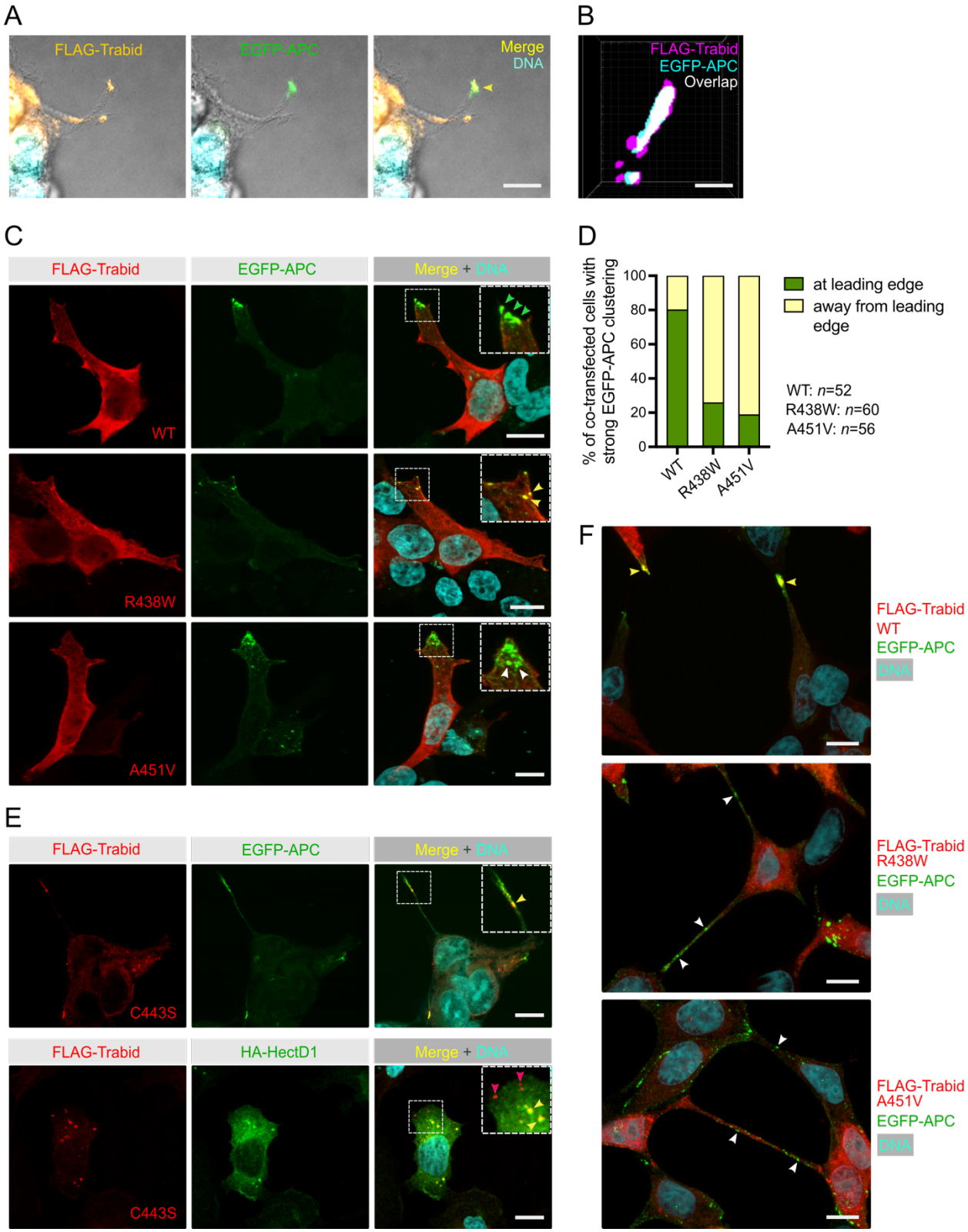
A
FLAG-Trabid
EGFP-APC
Merge
DNA
B
FLAG-Trabid
EGFP-APC
Overlap
C
FLAG-Trabid
EGFP-APC
Merge + DNA
WT
R438W
A451V
D
% of co-transfected cells with strong EGFP-APC clustering
100
80
60
40
20
0
WT
R438W
A451V
at leading edge
away from leading edge
WT: n=52
R438W: n=60
A451V: n=56
E
FLAG-Trabid
EGFP-APC
Merge + DNA
C443S
FLAG-Trabid
HA-HectD1
Merge + DNA
C443S
F
FLAG-Trabid
WT
EGFP-APC
DNA
FLAG-Trabid
R438W
EGFP-APC
DNA
FLAG-Trabid
A451V
EGFP-APC
DNA

822

823 **Figure 5. Trabid patient mutants impede the transport of EGFP-APC to the leading edge**
824 **of migrating cells.**
825 **A**. Combined differential interference contrast and immunofluorescence images of HEK293T
826 cells extending long cell processes that contain FLAG-Trabid and EGFP-APC in the cortical
827 protrusions of co-transfected cells (arrowhead in merged image). Scale bar, 10 μm.
828 **B**. 3D-SIM super resolution microscopy analysis of HEK293T cell tip clusters (n=5) revealed
829 ~30% overlap of FLAG-Trabid and EGFP-APC signals at resolutions of ~100 nm in *xy* and 320
830 nm in *z*. Scale bar, 100 nm.
831 **C**. EGFP-APC membrane clusters at the leading edge of migrating HEK293T cells (green
832 arrowheads) are readily detected with FLAG-Trabid wild-type co-expression. In cells expressing
833 FLAG-Trabid patient mutants, EGFP-APC aggregate in punctate structures near the leading edge
834 (white arrowheads), that are often sequestered together with the FLAG-Trabid R438W mutant
835 (yellow arrowheads). Scale bar, 10 μm.
836 **D**. Quantification of strong EGFP-APC clustering at or away from the leading edge membrane of
837 co-transfected HEK293T cells, as shown in C. Numbers of cells analysed from 3 independent
838 transfections are shown.
839 **E**. In co-transfected HEK293T cells, DUB-dead FLAG-Trabid C443S form puncta that
840 sequesters EGFP-APC near the tips of long cell protrusions or sequesters HA-HECTD1 in the
841 cytoplasm (yellow arrowheads). Notably, HA-HECTD1 was not detected in FLAG-Trabid
842 C443S puncta that form near the leading edge membrane of migrating cells (red arrowheads).
843 Scale bar, 10 μm.
844 **F**. In near-confluent HEK293T cells 48h post transfection, FLAG-Trabid patient mutants induce
845 long thin tubes that connect neigbouring cells and extensive EGFP-APC aggregations are
846 conspicuous along these tubular structures. This phenomenon was not observed in cells
847 transfected with wild-type FLAG-Trabid. Scale bar, 10 μm.
848
849
850
851
852

Figure 6

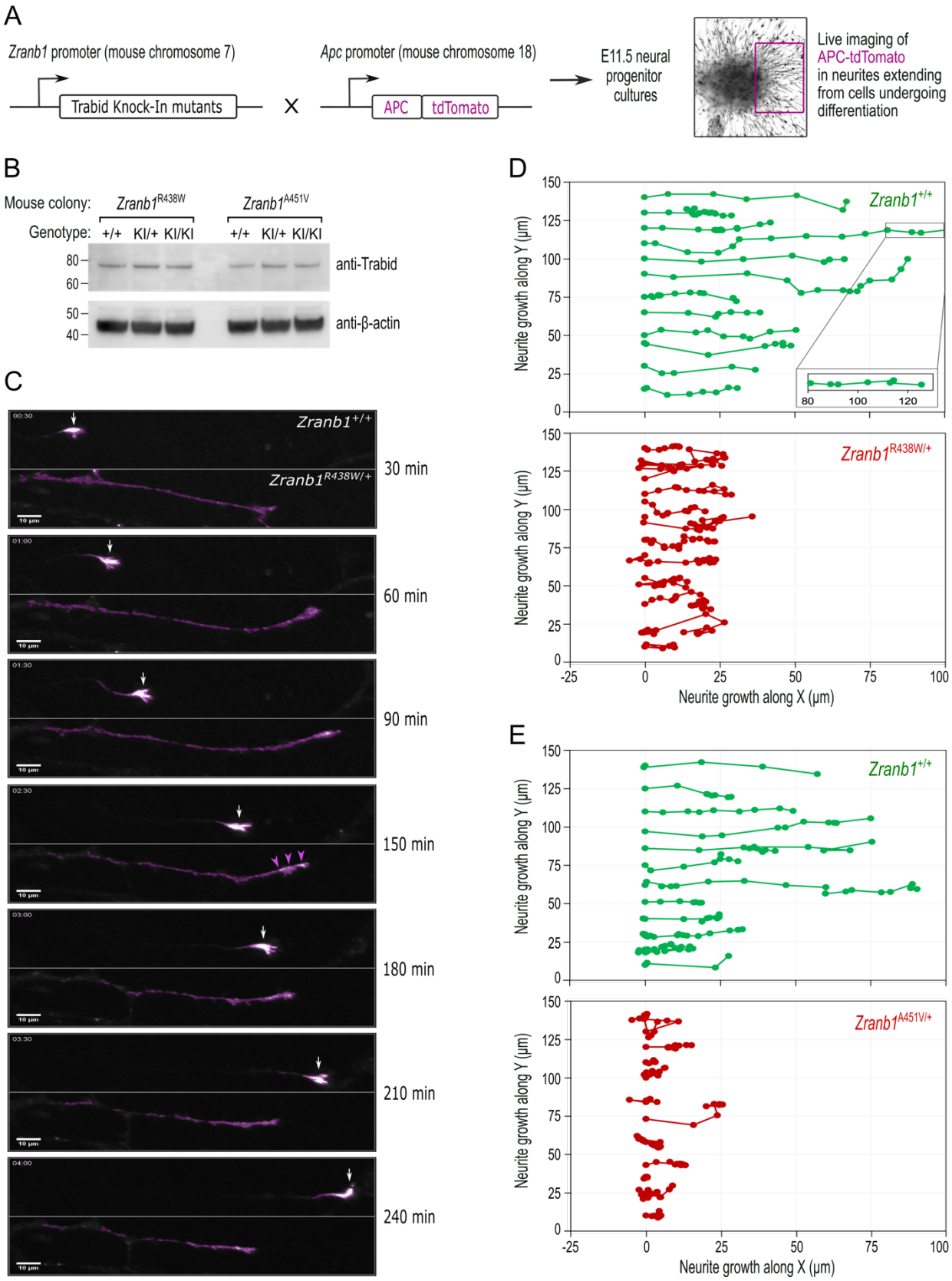
A
Zranb1 promoter (mouse chromosome 7)
Trabid Knock-In mutants
X
Apc promoter (mouse chromosome 18)
APC
tdTomato
E11.5 neural progenitor cultures
Live imaging of APC-tdTomato in neurites extending from cells undergoing differentiation
B
Mouse colony:
Zranb1R438W
Zranb1A451V
Genotype:
+/+ KI/+ KI/KI
+/+ KI/+ KI/KI
80
60
50
40
anti-Trabid
anti-β-actin
C
Zranb1+/+
Zranb1R438W/+
30 min
60 min
90 min
150 min
180 min
210 min
240 min
D
Zranb1+/+
Zranb1R438W/+
Neurite growth along Y (µm)
Neurite growth along X (µm)
E
Zranb1+/+
Zranb1A451V/+
Neurite growth along Y (µm)
Neurite growth along X (µm)

853

854 **Figure 6. Trabid patient mutations perturb the trafficking of APC-tdTomato and the**
855 **trajectory of neurite outgrowth.**
856 **A**. Schematic of outcross between knock-in mice harbouring *Zranb1/Trabid* patient mutations
857 and *Apc*^{tdTomato} mice, where the APC-tdTomato fluorescent protein is expressed under the control
858 of the endogenous *Apc* gene promoter. Midbrain neural progenitors derived from E11.5 embryos
859 of these outcrosses were used for live cell imaging of APC-tdTomato trafficking in growing
860 neurites.
861 **B**. Western blot analysis of Trabid protein expression in E11.5 midbrain neural progenitors
862 derived from heterozygous intercrosses in the *Zranb1/Trabid* R438W or A451V mouse colonies.
863 Mutant Trabid protein levels are expressed at comparable levels to wild-type Trabid protein
864 (compare KI/KI to +/+).
865 **C**. Live cell imaging of APC-tdTomato in neurites extending from E11.5 midbrain neural
866 progenitors of a *Zranb1*$^{R438W/+}$;*Apc*$^{tdTom/+}$ outcross. The frames shown are from a 4h time lapse
867 portraying the movement of APC-tdTomato. APC-tdTomato accumulated in the tips of neurites
868 with wild-type Trabid (*Zranb1*$^{+/+}$) to generate growth cones that drive axon elongation (white
869 arrows). In neurons with mutant Trabid (*Zranb1*$^{R438W/+}$; *Zranb1*$^{A451V/+}$ data not shown), APC-
870 tdTomato intensities were broadly distributed along neurites (purple arrowheads) and the
871 formation of growth cones was abrogated. Scale bar, 10 μm.
872 **D** and **E**. The movement of Apc-tdTomato in individual neurite tips was tracked to visualize
873 growth trajectory. Neurites extending from E11.5 midbrain neural progenitors of
874 *Zranb1*$^{R438W/+}$;*Apc*$^{tdTom/+}$ (D) or *Zranb1*$^{A451V/+}$;*Apc*$^{tdTom/+}$ (E) outcrosses were analysed. Each data
875 point represents the location of APC-tdTomato at 15-min intervals of a 4h time lapse. APC-
876 tdTomato fluorescence synchronised with the movement of a membrane dye during neurite
877 extension/retraction (data not shown) and was therefore used as a proxy for neurite growth along
878 an arbitrary X and Y plane. Neurite tracking data were compiled from the imaging of neurite
879 outgrowth in 3 independent neurosphere cultures established from E11.5 embryos of 3
880 independent *Zranb1*$^{R438W/+}$;*Apc*$^{tdTom/+}$ or *Zranb1*$^{A451V/+}$;*Apc*$^{tdTom/+}$ outcrosses. All image
881 acquisition, processing and analyses were performed blinded to genotype.
882
883
884

Figure 7

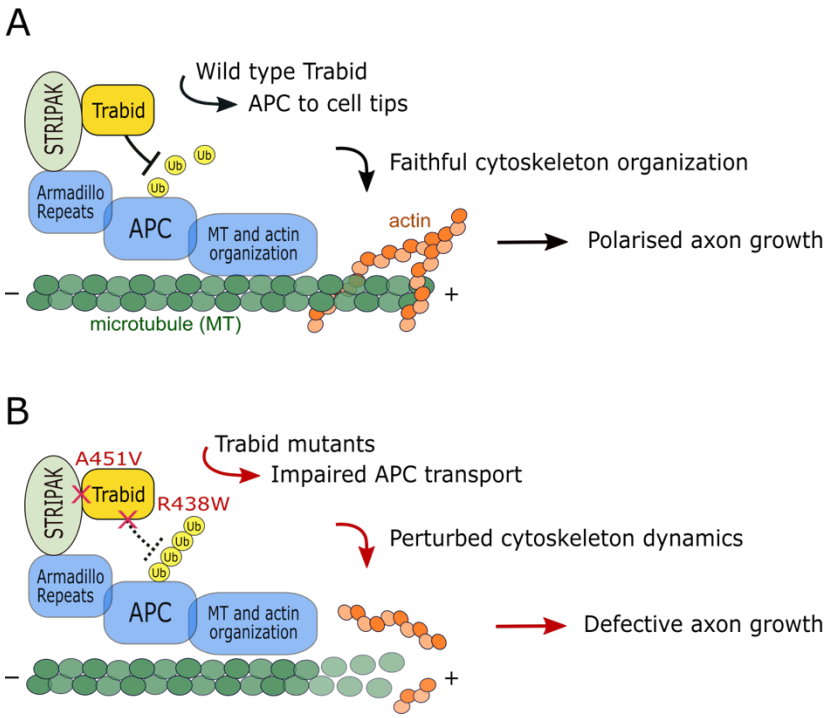

Figure 7. Model of Trabid's mechanism of action in axon growth and guidance.

A. STRIPAK recruits Trabid to deubiquitylate APC (and possibly other substrates). This promotes efficient APC accumulation at microtubule plus ends to coordinate the actin and microtubule cytoskeleton dynamics that drive directional cell migration and polarised axon growth.

B. In cells expressing Trabid mutants that are DUB-impaired (R438W) or STRIPAK-binding-deficient (A451V), APC becomes persistently modified with ubiquitin chains that retard its transport to cell tips. This impairs cytoskeleton organisation which leads to defective axon elongation and cell migration. Future studies will aim to identify the mechanism of Trabid recruitment to STRIPAK, the ubiquitin-modified residue(s) on APC (and possibly other substrates), and the composition of polyubiquitin linkages on substrates including the Lys29- and Lys33-linked atypical chain types preferentially targeted by Trabid.